Article

A singlet-triplet hole-spin qubit in MOS silicon

S. D. Liles [1] ✉, D. J. Halverson[1], Z. Wang[1], A. Shamim[1], R. S. Eggli [2], I. K. Jin[1,3], J. Hillier[1], K. Kumar[1], I. Vorreiter [1], M. J. Rendell [1], J. Y. Huang [4,5], C. C. Escott[4,5], F. E. Hudson [4,5], W. H. Lim[4,5], D. Culcer [1], A. S. Dzurak [4,5] & A. R. Hamilton [1]

Holes in silicon quantum dots are promising for spin qubit applications due to the strong intrinsic spin-orbit coupling. The spin-orbit coupling produces complex hole-spin dynamics, providing opportunities to further optimise spin qubits. Here, we demonstrate a singlet-triplet qubit using hole states in a planar metal-oxide-semiconductor double quantum dot. We demonstrate rapid qubit control with singlet-triplet oscillations up to 400 MHz. The qubit exhibits promising coherence, with a maximum dephasing time of 600 ns, which is enhanced to 1.3 μs using refocusing techniques. We investigate the magnetic field anisotropy of the eigenstates, and determine a magnetic field orientation to improve the qubit initialisation fidelity. These results present a step forward for spin qubit technology, by implementing a high quality singlet-triplet hole-spin qubit in planar architecture suitable for scaling up to 2D arrays of coupled qubits.

Silicon metal-oxide-semiconductor (MOS) quantum dots offer a compelling platform for implementing quantum circuits due to their compatibility with existing semiconductor foundry processes[1,2]. A leading approach for developing silicon qubits are silicon spin-qubits, due to their extended coherence times, minimal device footprint, and the potential for high integration densities[3]. The most straightforward implementation of a spin qubit uses single-spins[4]. This qubit encodes information using the $|\uparrow\rangle$ and $|\downarrow\rangle$ spin states of a localised electron. However, the adaptability of semiconductor quantum dot technologies permits a range of spin qubit implementations, each with unique advantages for quantum technology[5].

The singlet-triplet qubit is an alternative form of spin qubit, which offers several advantages for implementation in scalable quantum circuits[6–9]. A singlet-triplet qubit uses the singlet ($S = (|\uparrow\downarrow\rangle - |\downarrow\uparrow\rangle)/\sqrt{2}$) and unpolarised-triplet ($T_0 = (|\uparrow\downarrow\rangle + |\downarrow\uparrow\rangle)/\sqrt{2}$) states of two exchange-coupled spins. While using two spins rather than one increases the fabrication footprint and the complexity of the eigenstates, singlet-triplet qubits offer specific advantages. Singlet-triplet qubits can be operated at very low magnetic fields (<5 mT), which enables

compatibility with magnetic-sensitive components such as super-conducting resonators[10–13]. Additionally, singlet-triplet qubits can be controlled using only baseband control pulses, with spectral components generally not exceeding 100 MHz. This reduces the cost and complexity of control hardware compared with single-spin qubits, which typically require GHz phase-controlled tones. Moreover, removing the need for GHz control tones is advantageous since high-frequency tones dissipate more power at the device than baseband pulses, and this extra power dissipation impacts qubit control fidelity[14–17].

Hole spins in Group IV materials offer significant opportunities for use as fast scalable spin qubits[18–22] because of the strong intrinsic spin–orbit coupling, which is vanishingly small for electron spins. The intrinsic spin–orbit coupling allows rapid electrical manipulation of hole-spin qubits with recent state-of-the-art demonstrations reaching control speeds in the sub-nanosecond range[23]. Importantly, this rapid control is possible without the need for additional bulky features such as micro-magnets or ESR strip-lines. Further, the g-factor[24–30] and spin–orbit coupling[31] for holes are both tunable, providing a wide range of in-situ control over hole-qubits. In addition, hole-spins have

[1]School of Physics, University of New South Wales, Sydney, NSW 2052, Australia. [2]Department of Physics, University of Basel, Klingelbergstrasse 82, CH-4056 Basel, Switzerland. [3]Center for Emergent Matter Science, RIKEN, 2-1, Hirosawa, Wako-shi 351-0198 Saitama, Japan. [4]School of Electrical Engineering and Telecommunications, University of New South Wales, Sydney, NSW 2052, Australia. [5]Diraq, Sydney, NSW, Australia. ✉e-mail: s.liles@unsw.edu.au
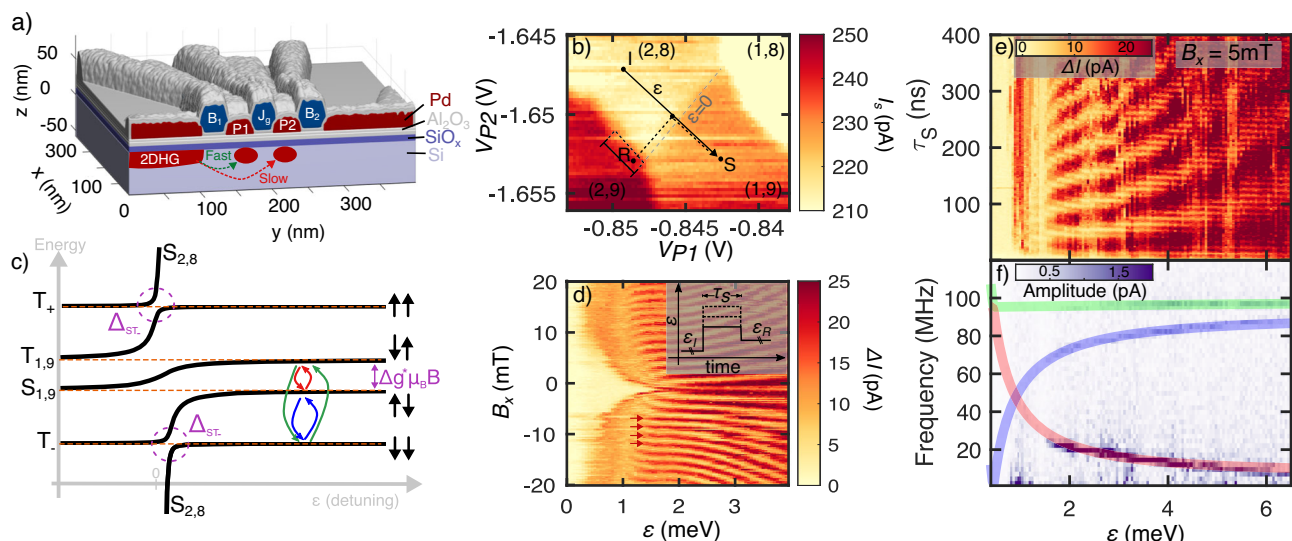
Fig. 1 | Device operating point and energy spectrum. a A 3D model of the device, showing a cross-section through the double quantum dot region. A full SEM image is shown in Supplementary Fig. 1. The tunnelling to the P1 dot was fast (<100 ns), while loading onto P2 dot was slow (>40 μs). This asymmetry in tunnelling allows latched readout. **b** Stability diagram of the (2,8)-(1,9) transition. The labels (N,M) indicate the number of holes in the P1 and P2 dot, respectively. The colour scale is the sensor current (I_s) in pA. Zero detuning ($\varepsilon = 0$) is defined as the (2,8) and (1,9) charge degeneracy point, and positive detuning when the spins are separated into (1,9). Full details of the pulse sequence are discussed in Supplementary Note 2. **c** Eigenstates calculated using the singlet-triplet Hamiltonian H_{ST} defined in Supplementary Note 4. The coloured arrows indicate the energy transitions observed in the preceding experiments, and Δ_{ST} indicates the size of the avoided crossing between $|S\rangle$ and $|T_\pm\rangle$. Orange dashed lines show how the (1,9) states evolve in the absence of spin−orbit coupling. **d** The results of a spin funnel experiment with the pulse sequence are shown in the inset. The spin-funnel experiment was performed by initialising $|S_{2,8}\rangle$, followed by a rapid pulse to a point along the detuning axis (ε). At each B_x and ε, the state was allowed to evolve for a fixed separation time, $\tau_s = 100$ ns, followed by a pulse to the readout point. The change in sensor signal (ΔI) due to this pulse indicates the likelihood of the returned state being singlet (low ΔI) or triplet (high ΔI) (described in more detail in the Methods). Red arrows indicate the Δg-driven oscillations. **e** The same pulse procedure as in d) except the magnetic field is fixed at $B_x = 5$ mT and we investigate the effect of varying the separation time (τ_S) at each detuning (ε). **f** The corresponding FFT at each detuning. Transparent lines indicated the best fit of the observed energy splittings to the eigenstates of H_{ST}, and the colours correspond to the transitions indicated in (**c**).

the potential for enhanced coherence times due to suppressed hyperfine coupling[32], and the potential for configuring decoherence sweet-spots by tuning the spin−orbit interaction[33−36].

Despite the opportunities holes offer, there currently are only limited studies of hole-based singlet-triplet qubits. Recently, a hole-spin singlet-triplet qubit was demonstrated in Ge[37], where the strong spin−orbit coupling resulted in non-trivial qubit dynamics[38]. However, the spin−orbit effects in Si devices vary from Ge devices. Most notably, the splitting between the heavy hole and light hole bands is typically an order of magnitude larger in planar Ge devices compared with planar Si devices[39,40]. Since the spin−orbit interaction is influenced primarily by the heavy hole light hole splitting, the spin−orbit-driven phenomena can vary significantly between the two material systems. For example, the ratio of the in-plane to out-of-plane g-factors observed in Ge is significantly larger than in Si[38]. Given the difference in spin−orbit effects between Ge and Si, investigations into Si are needed to provide an understanding of Si holes.

Recent experiments in silicon FinFET's have revealed an anisotropic exchange coupling for holes due to the spin−orbit interaction[41], which may provide unique functionalities for hole-spin singlet-triplet qubits. Indeed, theoretical predictions have suggested that the non-trivial relationship between spin−orbit coupling and the site-dependent g-tensors may allow hole-spin singlet-triplet qubits to avoid leakage errors[42]. However, to-date, there are no demonstrations of a singlet-triplet qubit using holes in silicon.

In this work, we demonstrate a hole-spin singlet-triplet qubit formed in a planar MOS silicon double quantum dot. The planar structure provides a platform suitable for scaling up to the large arrays of coupled qubits needed for quantum circuits and error correction[43−45]. We identify the exact hole occupation of the double dot, which is critical for experimental reproducibility and detailed

theoretical modelling of this system. In addition to characterising the key parameters of the qubit, we perform an investigation into the anisotropy of the two-hole eigenstates. By comparing the experimental results with a model that includes spin−orbit coupling and anisotropic site-dependent g-tensors, we identify key features in the eigenstates that allow the improvement of the initialisation fidelity and reduction in the readout errors.

Results
Device and operating regime
The hole-spin singlet-triplet qubit is formed using a planar-silicon double quantum dot device, fabricated using industrially compatible CMOS techniques. Figure 1a shows a model 3D cross-section of the double quantum dot region. Multi-layer palladium gates define the double quantum dot with P1 and P2 operating as plunger gates, while J_g provides in-situ control of the interdot tunnel coupling t_c[46]. The device employs ambipolar charge sensing[47], with an adjacent *n*MOS SET allowing the absolute charge occupation of each quantum dot to be determined.

Figure 1b shows a stability diagram measured using the charge sensor. We perform all measurements in the (2,8)-(1,9) configuration, which is equivalent to a (2,0)-(1,1) spin system due to orbital shell filling[48]. We initialised singlet states by dwelling deep in (2,8) where $|S_{2,8}\rangle$ is the lowest energy eigenstate (point I). Manipulation of the state was performed by pulsing to a position along the detuning axis (ε) and dwelling there for a variable time τ_s. Readout of the state was performed by pulsing to point R (following the dashed trajectory), where latched Pauli−Spin−Blockade[49,50] readout allowed identification of either the blocked triplet or the unblocked singlet states based on the average sensor current (see Methods and Supplementary Notes 1−3).

System Hamiltonian and eigenenergies

To model the two-spin system, we consider a 5×5 Hamiltonian, H_{ST}, which includes Zeeman, spin–orbit and orbital terms. The full details of the two-hole singlet-triplet Hamiltonian are provided in Supplementary Note 4. For the Zeeman Hamiltonian, we include independent 3×3 symmetric g-tensors for the left and right dot, $\overset{\leftrightarrow}{g}_L$ and $\overset{\leftrightarrow}{g}_R$, respectively. Hole-spins in silicon are known to have strongly anisotropic g-tensors[25–27,41], where variations in the g-tensor are produced by non-uniform strain[27,29], spin–orbit coupling[30] and differences in the confinement profile between the two dots[24]. Hence, we do not assume that $\overset{\leftrightarrow}{g}_L$ and $\overset{\leftrightarrow}{g}_R$ are correlated or share the same principle spin-axes. For the spin–orbit Hamiltonian we include a spin–orbit vector, $\mathbf{t}_{so} = (t_x, t_y, t_z)$, parameterising the effect of spin–orbit coupling in the laboratory reference frame indicated in Fig. 1a.

In Fig. 1c, we plot the eigenenergies of H_{ST} as a function of detuning. At negative detuning, the eigenstates are the $(|T_+\rangle, |T_0\rangle, |T_-\rangle, |S\rangle, |S_{2,8}\rangle)$ basis states. At large positive detuning, the eigenstates evolve into the $|S_{2,8}\rangle$ state and the four two-spin states $(|\uparrow\uparrow\rangle, |\uparrow\downarrow\rangle, |\downarrow\uparrow\rangle, |\downarrow\downarrow\rangle)$, which are defined by the sum or difference of the Zeeman energy in the two dots. The $|\uparrow\downarrow\rangle$ and $|\downarrow\uparrow\rangle$ eigenstates have energy splitting given by

$$E_{ST_0} = \sqrt{J(\epsilon, t_c)^2 + \Delta E_Z^2} \qquad (1)$$

where

$$J(\epsilon) = \sqrt{\frac{\epsilon^2}{4} + 2t_c^2} - \frac{\epsilon}{2} \qquad (2)$$

$$\Delta E_Z = |\Delta g^*|\mu_B|\mathbf{B}| \qquad (3)$$

ϵ is the detuning energy, t_c is the interdot tunnel coupling, Δg^* is the difference in the effective g-factors for the applied magnetic field vector $\mathbf{B}$ (see Supplementary Note 4), and μ_B is the Bohr magneton. Since strong spin–orbit coupling results in an anisotropy in $|\Delta g^*|$ with respect to magnetic field orientation, we expect E_{ST_0} to exhibit a non-trivial anisotropy[41]. An avoided crossing occurs between the $|S_{2,8}\rangle$ and $|T_\pm\rangle$, with the amplitude of the avoided crossing ($\Delta_{ST_\pm}$) determined by the interplay between the spin–orbit vector and the difference in the projection of the g-tensors for the given field orientation[38].

Figure 1d shows the charge sensor response of a spin-funnel experiment used to characterise the singlet-triplet system[7]. The spin-funnel experiment was performed by allowing a singlet state to time-evolve for $\tau_s = 100$ ns at each B_x and ϵ. The change in sensor signal (ΔI) then measures the likelihood that the final state is either singlet (low ΔI) or triplet (high ΔI). A clear funnel edge is visible in ΔI when the detuning point coincides with the $|S\rangle$ and $|T_\pm\rangle$ avoided crossing[7]. In addition, on the positive detuning side of the funnel edge, we see oscillations that result from Δg-driven $|S\rangle \leftrightarrow |T_0\rangle$ oscillations (red arrows).

Figure 1e demonstrates the time evolution of the singlet at each detuning. The experimental procedure is the same as Fig. 1d, however here we varied the separation time (τ_S) at each detuning (ϵ) and held the magnetic field constant at $B_x = 5$ mT. Figure 1f shows the FFT of ΔI at each ϵ, revealing three clear oscillation frequencies, each with a distinct detuning dependence. Each oscillation frequency results from mixing between the three lowest eigenstates at the separation detuning (ϵ). The lowest frequency (red) results from oscillations between $|S\rangle \leftrightarrow |T_0\rangle$ states, the middle frequency (blue) results from oscillations between $|S\rangle \leftrightarrow |T_\pm\rangle$, and the highest frequency (green) results from oscillations between $|T_0\rangle \leftrightarrow |T_\pm\rangle$. The corresponding transitions are indicated by coloured arrows in Fig. 1c and a full description is provided in the methods.

We fit the observed frequencies in Fig. 1f to the eigenergies of the singlet-triplet Hamiltonian, H_{ST} and extract key parameters of the two-hole system. Transparent lines in Fig. 1f show the best fit,

demonstrating good agreement between the observed and theoretical eigenenergies. Based on the best fit, we extract $t_c = 9 \pm 1$ µeV and two effective g-factors of 0.8 ± 0.1 and 1.2 ± 0.1 for B_x.

Anisotropic g-tensors and spin–orbit coupling

To characterise the key parameters of the two-hole system, we investigate the effect of magnetic field orientation on the two-hole eigenergies. Figure 2a shows ΔI as a function of τ_S for a range of magnetic field orientations in the x-z plane, and Fig. 2b shows the resulting FFT of ΔI. Figure 2c, d repeat the same experiment for a rotation of the magnetic field through the x-y plane. Clear anisotropy with respect to magnetic field orientation can be observed, which results from the interplay between spin–orbit coupling and the orientation of the g-tensors. The visibility of the higher frequency (blue and green) oscillations also shows a strong dependence on the magnetic field orientation. In particular, the FFT amplitude of the higher frequency (blue and green) oscillations is suppressed for B_x and enhanced for B_y and B_z.

The 3×3 g-tensors for each dot and the spin–orbit orientation can be extracted by fitting the data in Fig. 2a–d to the eigenergies of H_{ST}. The fitting procedure is discussed in the methods and Supplementary Notes 7, 8. The transparent lines in Fig. 2b, d indicate the frequency of the respective FFT peaks for the optimal fit parameters. For the optimal fit we find $(t_{so}^x, t_{so}^y, t_{so}^z) = (-37 \pm 2, 107 \pm 4, 0 \pm 20)$ neV, giving $|\mathbf{t}_{so}| = 0.12$ µeV. Notably, $\mathbf{t}_{so}$ is oriented in-plane with the 2DHG, consistent with expectations for heavy holes in planar silicon[51]. Further, the in-plane spin–orbit vector has components in both t_{so}^x and t_{so}^y, indicating that a combination of Rashba (oriented perpendicular to the double dot axis) and Dresselhaus (oriented parallel to the double dot axis) spin–orbit components are present[52]. The full g-tensors are presented in the methods. We find that the orientation of the g-tensor principle axes for left and right dots are slightly misaligned, which may result from differences in confinement profile or non-uniform strain between the left and right dots. The observation of misalignment in the g-tensor principle axes suggests accurate modelling of multiple quantum dot systems in silicon should incorporate site-dependent g-tensors with differing principle axes.

The anisotropy in the FFT amplitudes in Fig. 2a–d is caused by the probability of transitioning from $|S_{2,8}\rangle$ into $|T_-\rangle$ during the pulse from (2,8) to (1,9). When pulsing from (2,8) to (1,9) the $\Delta_{ST_\pm}$ avoided crossing causes the initial $|S_{2,8}\rangle$ state to be split between $|S\rangle$ and $|T_-\rangle$ with a ratio determined by the Landau–Zener transition probability[53] (see methods and Supplementary Note 6). Larger $\Delta_{ST_\pm}$ favours $|T_-\rangle$ states, while smaller $\Delta_{ST_\pm}$ favours $|S\rangle$. In Fig. 2e, we plot the energy spectrum of the two-hole system for various in-plane magnetic field orientations. The magnetic field orientation strongly influences the magnitude of $\Delta_{ST_\pm}$ and the position in detuning (ϵ_Δ) at which the avoided-crossing occurs. As a result, the magnetic field orientation impacts the likelihood of populating the $|T_-\rangle$ state during the separation ramp and thus impacts the amplitude of the $|S\rangle \leftrightarrow |T_-\rangle$ FFT peak.

We simulated the experimental pulse sequence using QuTIP[54] and calculated the $|S_{2,8}\rangle \rightarrow |T_-\rangle$ transition probability (P_{T_-}), which yielded good agreement with the measured FFT amplitude. In Fig. 2f, the solid line shows the calculated P_{T_-} using the optimal fit parameters for a range of in-plane magnetic field orientations (See Supplementary Note 7 for details). The circles in Fig. 2f show the observed amplitudes of the $|S\rangle \leftrightarrow |T_-\rangle$ FFT peaks from Fig. 2d (blue). The trend in P_{T_-} matches the anisotropy in the measured amplitudes of the $|S\rangle \leftrightarrow |T_-\rangle$ FFT peaks from Fig. 2d, with both exhibiting a peak around $\theta = 120°$, and an asymmetric reduction towards $0°$ and $180°$. The correlation between FFT amplitude and the calculated P_{T_-} demonstrates that the model H_{ST} and optimal fit parameters capture the dynamics of the hole-spin qubit well (see Methods).

We now consider how hole-spin singlet-triplet qubits can be further optimised by using the anisotropic response of the system to a magnetic field. For the singlet-triplet qubit studied here, an optimal initialisation protocol would suppress the likelihood of the $|S_{2,8}\rangle$ state
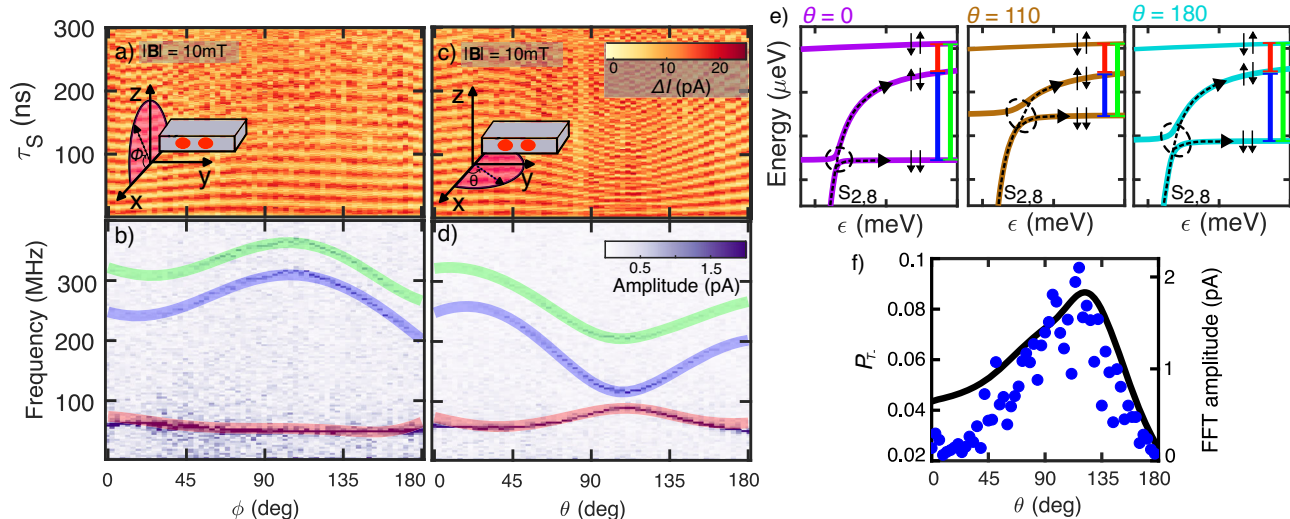
Fig. 2 | Eigenenergy anisotropy with respect to magnetic field orientation. **a**, **b** Shows the sensor signal and resulting FFT when using the pulse sequence given in Fig. 1d) (initialise-separate-readout). Detuning is fixed at $\epsilon = 1.9$ meV and a 10 mT magnetic field is rotated by 180° through the x-z plane. **c**, **d** Shows the same experiment for a rotation through the sample x-y plane. Transparent solid lines show the optimal fit of H_{ST} to the experimental data, and a zoom-in of the first 60 ns of (**c**) is reproduced later in the Methods, highlighting the multiple frequencies present. See Supplementary Note 5 for the full 360° data set in the x-y plane. **e** Shows the eigenenergies for $|B| = 10$ mT magnetic field applied at $\theta = 0°$ (purple), 110° (brown) and 180° (cyan) in the x-y plane, respectively. The y-axis ticks are in 0.5 μeV, and the x-axis ticks are separated by 1 meV. The energy splitting corresponding to the three FFT peaks in (**d**) are indicated by the red, blue and green vertical lines. The size and location of the $|S\rangle$-$|T_-\rangle$ avoided crossing varies with field orientation (black dashed circle), resulting **b** anisotropy in the Landau–Zener transition probability between $|S_{2,8}\rangle \rightarrow |T_-\rangle$ during the ramp-in/ramp-out. The black dashed lines indicated the splitting of the initial state when pulsing across the Δ_{ST} avoided crossing. **f** The solid black line is the calculated probability of the $|S_{2,8}\rangle$ loading into $|T_-\rangle$ during the separation pulse (P_{T_-}, left axis). Blue markers indicate the amplitude of the $|S\rangle \leftrightarrow |T_-\rangle$ FFT peak in (**d**) (transparent blue). Both data were plotted as a function of the in-plane magnetic field angle. The trend in P_{T_-} correlates with the amplitude of the $|S\rangle \leftrightarrow |T_-\rangle$ oscillations in (**d**). The correlation between P_{T_-} and the $|S\rangle \leftrightarrow |T_-\rangle$ oscillation amplitude is expected since the $|S\rangle \leftrightarrow |T_-\rangle$ oscillations are enhanced as the probability of loading the $|T_-\rangle$ state increases.

loading into the $|T_-\rangle$ leakage state. In the presence of large spin–orbit coupling and/or large Δg, even rapid separation pulses may be unable to satisfy the non-adiabatic Landau–Zener requirement imposed by the large Δ_{ST_-} avoided crossing. However, with knowledge of the orientation of spin–orbit vector ($\mathbf{t}_{so}$), and the g-tensors, we can identify optimum field orientations to minimise Δ_{ST_-} and thus enhance the initialisation fidelity. Indeed, in Fig. 2f we have shown that the B_x magnetic field suppresses loading into the $|T_-\rangle$ state, and therefore is an optimal field orientation for the singlet-triplet qubit in this system.

Finally, we comment on the implications of the fitting procedure used. Here we demonstrate a method that is able to characterise the two arbitrary g-tensors and the spin–orbit vector without the need for GHz EDSR tones that are typically used[25,41]. The fitting approach, which is described in detail in the methods and Supplementary Notes 7, 8, leverages both the observed eigenenergies (FFT frequencies) and occupation probabilities (FFT amplitudes) in order to determine an optimal fit. While, we note that this method does not acquire a unique fit, we highlight that the optimal fits is sufficient to accurately reproduce the key qubit dynamics (see methods). Therefore this approach provides a method for extracting key qubit parameters for devices where EDSR is either not possible (such as in the very low magnetic field regime) or not available.

Coherent Δg-driven oscillations
We now turn to experiments to characterise the hole-spin qubit. Here, the qubit is defined using the $|S\rangle$ and $|T_0\rangle$ states of the double quantum dot. The simplified Hamiltonian for this system can be written as

$$H_{ST} = \frac{J}{2}\sigma_z + \frac{\Delta E_Z}{2}\sigma_x \qquad (4)$$

where J defines the exchange energy, $\Delta E_Z = |\Delta g^*|\mu_B|\mathbf{B}|$, $|\mathbf{B}|$ is the magnitude of the applied field vector, $\sigma_{x,z}$ are the respective Pauli matrices

and μ_B is the Bohr magneton. The Bloch sphere for this qubit system is shown in Fig. 3a. Rotations around the Bloch sphere can be driven by controlling J and ΔE_Z at the separation point[9,55], and Fig. 3b shows a schematic of the pulse sequence used.

Figure 3c plots the measured singlet probability P_S as a function of separation time τ_S for three different $|B_x|$, demonstrating oscillations in P_S. Solid lines in Fig. 3b show the best fit of the data to the equation

$$P_S = A\cos(2\pi f_R\tau_s + \phi)\exp\left[\left(\frac{\tau_s}{T_2^*}\right)^\alpha\right] + C \qquad (5)$$

where f_R is the Rabi frequency, τ_s is the separation time, ϕ is a phase offset, T_2^* is the qubit dephasing time, A is the oscillation amplitude, C is an offset, and α captures the noise colour (see Supplementary Note 5).

Analysis of the $|S\rangle \leftrightarrow |T_0\rangle$ oscillations over a range of B_x was used to characterise the qubit control frequency (f_R) and the coherence time (T_2^*). Figure 3d, e show a colour map of the $|S\rangle \leftrightarrow |T_0\rangle$ oscillations and a corresponding FFT at each B_x. We resolve $|S\rangle \leftrightarrow |T_0\rangle$ oscillations up to 150 MHz at 30 mT and have observed up to 400 MHz at 80 mT (Supplementary Note 5). To extract Δg and J we fit f_R for each B_x to Eqn. (1). The fit yields $J = 6$ MHz at the separation point ($\epsilon = 1.9$ meV), and $|\Delta g| = 0.41$ which is in agreement with the effective g-factors extracted from Fig. 1f. In Supplementary Note 5, we show electrical control over Δg^* using the J_g gate, with a trend of $d\Delta g^*/dJ_g \approx 0.9$ V^{-1}, demonstrating in-situ electrical control of the qubit control frequency.

We now show the decoherence in this qubit can be explained by fluctuations in both ϵ and ΔE_Z and we quantify their magnitudes. Figure 3f shows T_2^* for a range of B_x, where each T_2^* has been extracted using a fit to Eqn (5). Dephasing is caused by fluctuations in the energy splitting between the $|S\rangle$ and $|T_0\rangle$ states[56] (Eqn (1)). Hence, the

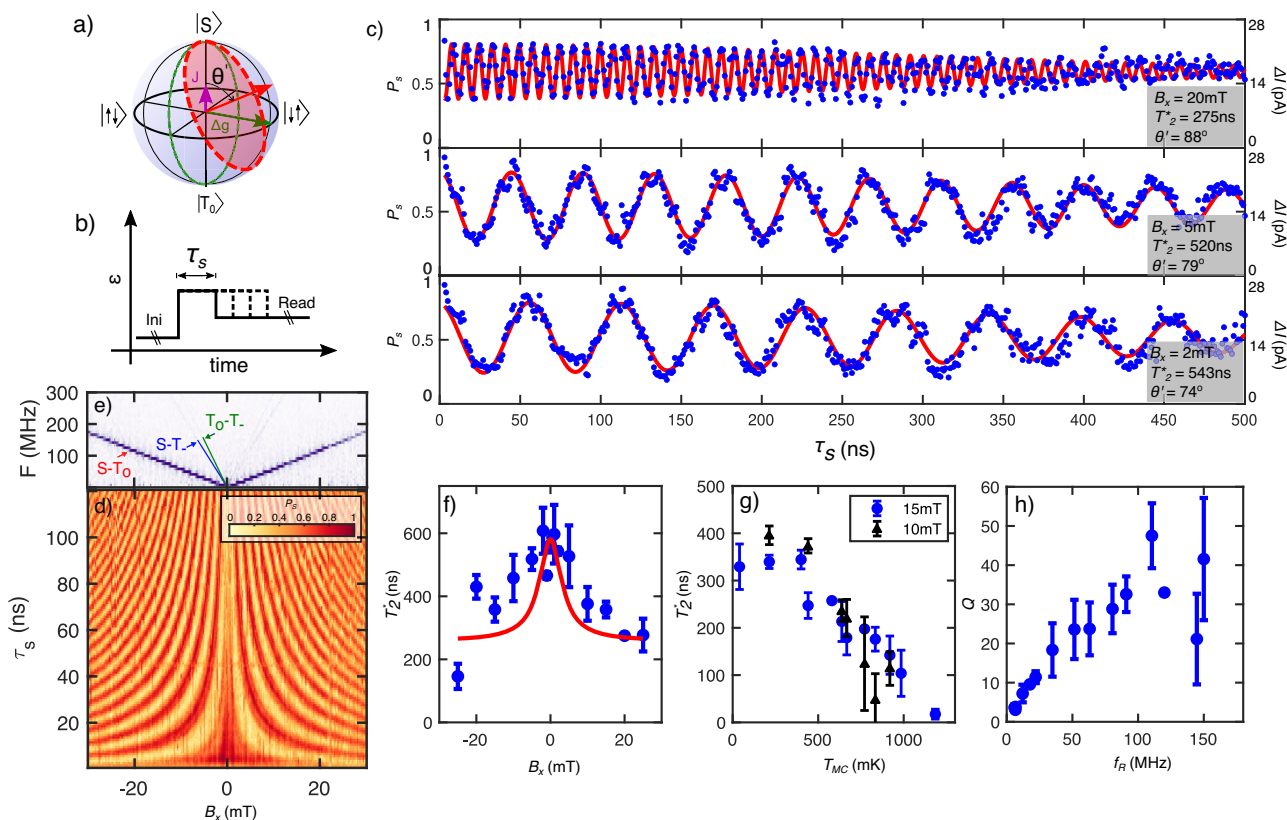**Fig. 3 | Δg-driven coherent oscillations. a** Shows a schematic of the Bloch sphere for the singlet-triplet qubit. The Zeeman energy difference ΔE_Z produces oscillations about the x-axis ($|S\rangle \leftrightarrow |T_0\rangle$ oscillations), while exchange coupling J produces oscillations about the z-axis (ie $|\uparrow\downarrow\rangle \leftrightarrow |\downarrow\uparrow\rangle$ oscillations). When both J and ΔE_Z are non-zero, the angle of rotation with respect to the Bloch sphere z-axis is given by $\theta' = \arctan(\frac{\Delta E_Z}{J})$ as indicated by the red trajectory. **b** Shows the pulse sequence used to drive the Δg-driven oscillations. We initialised in $|S_{2,8}\rangle$, then applied a rapid separation pulse along the detuning axis. The system was then held at a fixed positive detuning (ϵ) for a separation time (τ_S), before performing readout. **c** Shows the observed $|S\rangle \leftrightarrow |T_0\rangle$ oscillations as a function of separation time, for $B_x = 20, 5$ and 2 mT. The solid red line is the best fit for Eqn. (5) to the data. The singlet probability, P_S, at each τ_S is extracted from the change in the normalised sensor signal ΔI (shown on the right axis, see Supplementary Note 3). **d** Shows the $|S\rangle \leftrightarrow |T_0\rangle$ oscillations over a field range of $B_x = \pm 30$ mT. **e** Shows the FFT of the oscillations observed in (**d**). A linear increase in the oscillation frequency is expected since $hf = \Delta E_{ST_0}$ (Eqn. (1)). The B_x magnetic field orientation was used for these experiments since it results in the least leakage into $|T_-\rangle$ (Fig. 2). However, residual loading of the $|T_-\rangle$ leakage state results in weak $|S\rangle \leftrightarrow |T_-\rangle$ (blue) and $|T_0\rangle \leftrightarrow |T_-\rangle$ (green) oscillations for B_x. **f** Shows the T_2^* for different magnetic fields, where the solid line is the best fit of Eqn. (6) to both this data and the data in Fig. 4e. **g** Shows the effect of mixing chamber temperature on T_2^* for two different magnetic fields. **h** The qubit quality factor (Q) as a function of the Δg-driven oscillation frequency (f_R), measured at $T_{MC} = 30$ mK. All data in Fig. 3 was collected with $J_g = 1.2$ V. Error bars in (**f**–**h**) are the standard deviation in the measured value.

variation in T_2^* can be modelled using

$$\frac{1}{T_2^*} = \frac{\pi\sqrt{2}}{h}\sqrt{\left(\frac{J}{E_{ST_0}}\frac{dJ}{d\epsilon}\delta\epsilon\right)^2 + \left(\frac{\Delta E_Z}{E_{ST}}\delta\Delta E_Z\right)^2} \quad (6)$$

where $\delta\epsilon$ is the noise in detuning and $\delta\Delta E_Z$ is the effective magnetic noise. A common fit of the data in Figs. 3f, 4d (discussed later) was used to extract $\delta\epsilon = 30\,\mu eV$ and $\delta\Delta E_Z = 4$ neV. These values are comparable to those previously reported for electrons in silicon devices[8,57,58] and for holes in planar Ge devices[37]. The similarity in $\delta\epsilon$ between holes in planar Si and planar Ge suggests that the highly disordered SiO_2 oxide does not significantly enhance the effect of charge noise compared to planar Ge heterostructures, where the quantum dot is buried tens of nanometres below the surface. Further, the similarity in $\delta\epsilon$ between this work in *p*MOS silicon and studies of electrons in *n*MOS silicon[58] suggests that the level of charge noise is not impacted by the polarity of the gate bias. Finally, we note that the magnetic noise ($\delta\Delta E_Z$) we measured appears to arise primarily from fluctuations in the Overhauser field, which is produced by the 5% residual ^{29}Si nuclei (see Supplementary Note 5). This indicates that hole-spin qubits may similarly benefit from isotopic enrichment[59].

In Fig. 3g, we plot T_2^* of the Δg-driven oscillations as a function of the fridge mixing chamber temperature (T_{MC}). T_2^* is approximately independent of T_{MC} up to 400 mK ($k_BT = 34\,\mu eV$), where T_2^* begins to drop. The T_2^* behaviour shows the same trend at $B_x = 15$ mT ($\Delta E_{ST_0} = 0.35\,\mu eV$) and $B_x = 10$ mT ($\Delta E_{ST_0} = 0.23\,\mu eV$). Interestingly, we find that the noise colour (α) appears to whiten as the temperature of the fridge increases, consistent with recent experiments in other hole-spin qubits[19] (see Supplementary Note 5).

Finally, in Fig. 3h, we show that the quality factor ($Q = f_R \times T_2^*$) of the Δg-driven singlet-triplet oscillations increases as the control speed increases. The quality factor quantifies the number of coherent oscillations that can be completed within the coherence time. A promising feature of this qubit is that Q increases with increasing f_R, indicating that the qubit control speed can be increased without degrading the quality.

Coherent exchange-driven oscillations

In order to achieve full control of the singlet-triplet qubit it is necessary to produce control pulses that allow access to the full 3D Bloch sphere. We use exchange-driven oscillations to rotate the qubit around the z-axis of the Bloch sphere. By combining Δg-driven (x-axis) and exchange-driven (z-axis) rotations, it is possible to achieve full control over the qubit Bloch sphere.
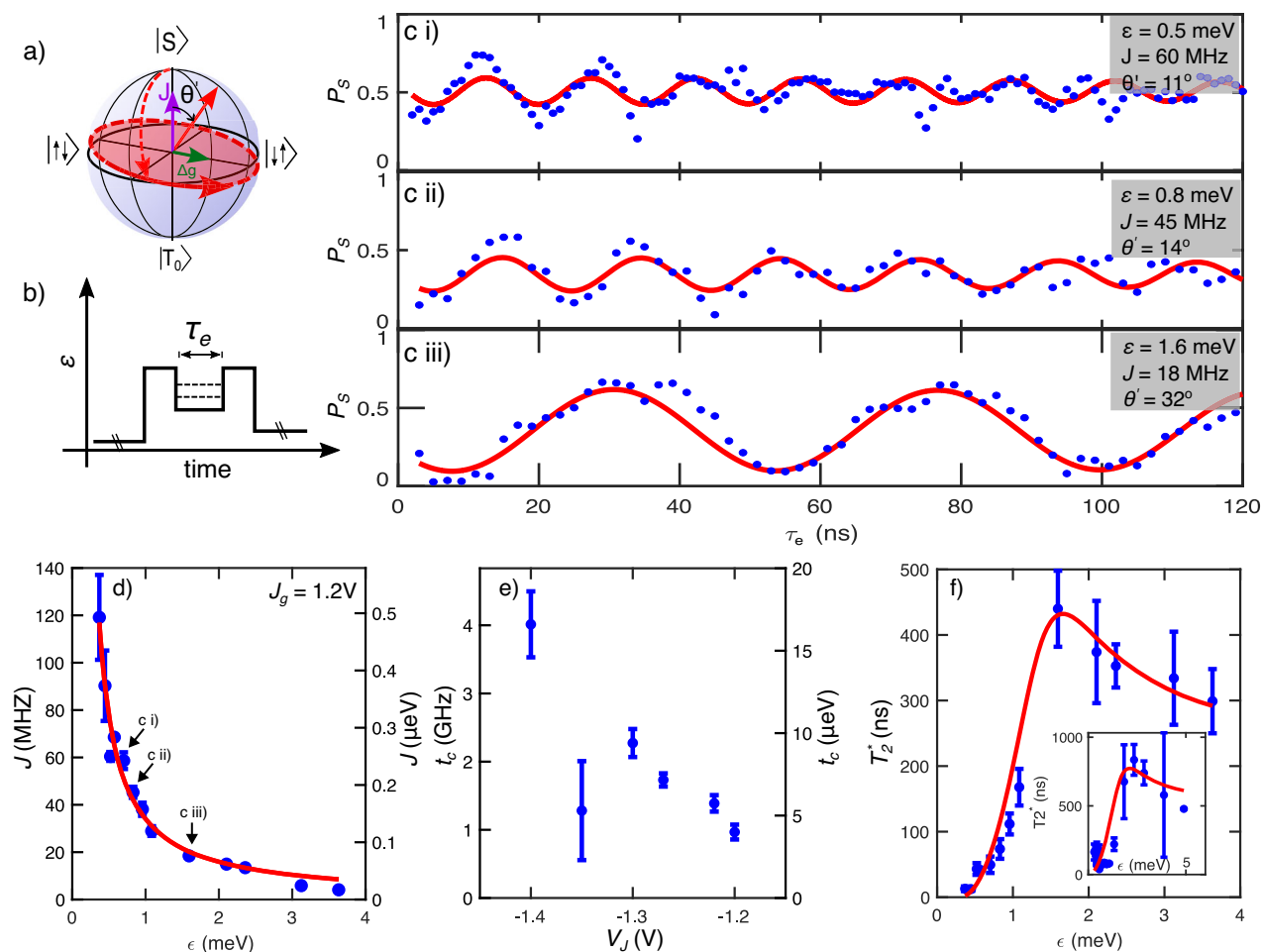
Fig. 4 | Exchange-driven coherent oscillations. a A schematic of the state evolution and **b** shows the pulse sequence used to achieve exchange-driven oscillations. A Δg-driven $\pi/2$ pulse brings the qubit to the equator (red dashed trajectory), then a rapid pulse to low detuning is used to suddenly increase J, changing the angle of rotation, resulting in exchange-driven oscillations around the equator (red trajectory). The orientation of the oscillation is tilted by θ' from the z-axis. **c** Exchange-driven oscillations for three different detunings ($\epsilon = 0.5, 0.8$ and 1.6 meV). Experiments were performed with a fixed magnetic field of $B_x = 2$ mT, such that a Δg-driven $\pi/2$ pulse takes 65 ns. The solid line shows a best fit to Eqn. (5), allowing extraction of J and T_2^* at each ϵ. **d** Exchange energy as a function of detuning, measured using the exchange pulse. The solid red lines show

the fit to $J(\epsilon, t_c) = \sqrt{\frac{\epsilon^2}{4} + 2t_c^2} - \frac{\epsilon}{2}$, allowing the extraction of the tunnel coupling t_c. **e** Tunnel coupling extracted for a range of different J_g gate voltages, where each t_c is extracted from the ϵ dependence of the exchange-oscillation frequency. The trend in t_c seems approximately linear in J_g (with the exception of an outlier at $J_g = -1.35$ V). While we would generally expect an exponential dependence of t_c on the J_g voltage, the linear response is consistent with previous data in silicon MOSFET structures[62]. **f** Dephasing time T_2^* as a function of the detuning. The solid red line is a joint fit of Eqn. (6) to this data and the data in Fig. 3f. All data in (**c, d, f**) was collected for $J_g = 1.2$ V, and the inset in (**f**) shows the dephasing time as a function of the detuning for $J_g = -1.4$ V. Error bars in (**d–f**) are the standard deviation in the measured value.

Figure 4a, b show the experimental procedure for exchange-driven oscillations. A separation pulse with calibrated τ_S is first used to perform a Δg-driven $\frac{\pi}{2}$ rotation to bring the state to the equator of the Bloch sphere. A rapid pulse to low detuning is then applied, which suddenly increases J, producing a change in the qubit rotation axis. The system is held at the exchange point for τ_E to drive oscillations around the z-axis, then a second Δg-driven $\frac{\pi}{2}$ rotation is applied, followed by a pulse to the readout position.

Figure 4c demonstrates exchange-driven oscillations at three different detuning position (ϵ). Reducing ϵ at the exchange position increases the exchange energy J, so that the angle of rotation tends towards 0° with respect to the Bloch sphere z-axis (since $J \gg \Delta g \mu_B B$). In Fig. 4d, we plot J as a function of ϵ at the exchange point. The solid line shows the best fit of $J(\epsilon, t_c)$, allowing the extraction of the tunnel coupling (see Figure caption). This experiment was repeated for a range of J_g gate voltages, and the resulting dependence of the tunnel coupling (t_c) on the J_g gate voltage is shown in Fig. 4e, demonstrating smooth control of t_c. Therefore, the exchange-driven oscillations are highly tunable, since J can be electrically tuned either by varying ϵ with

the plunger gates, or by tuning t_c using the J_g-gate. These results demonstrate coherent exchange-driven z-axis control of the singlet-triplet qubit.

Figure 4f presents T_2^* as a function of ϵ, which is used to characterise the coherence time of the exchange oscillations. The solid line shows the best fit to Eqn. (6), obtained by jointly fitting Figs. 4e, 3f. The trend in T_2^* is well explained by Eqn. (6), where charge noise ($\delta\epsilon$) dominates at low detuning due to enhanced $dJ/d\epsilon$, while Zeeman noise ($\delta\Delta E_Z$) dominates at large detuning where $dJ/d\epsilon \to 0$.

Spin-echo measurement

Finally, we investigate the use of spin-refocusing to enhance the qubit coherence time. Given that J and ΔE_Z are non-zero, rotations around the Bloch sphere occur at some angle offset from the pure x-axis or z-axis. Since the qubit trajectory is not solely around the x-axis or z-axis, the precise form of the refocusing pulse will vary as the qubit evolves. Therefore, complicated pulse engineering is required for perfect refocusing pulses[60]. Here, we implement a simplified procedure[37], which employs a π rotation using an exchange pulse to
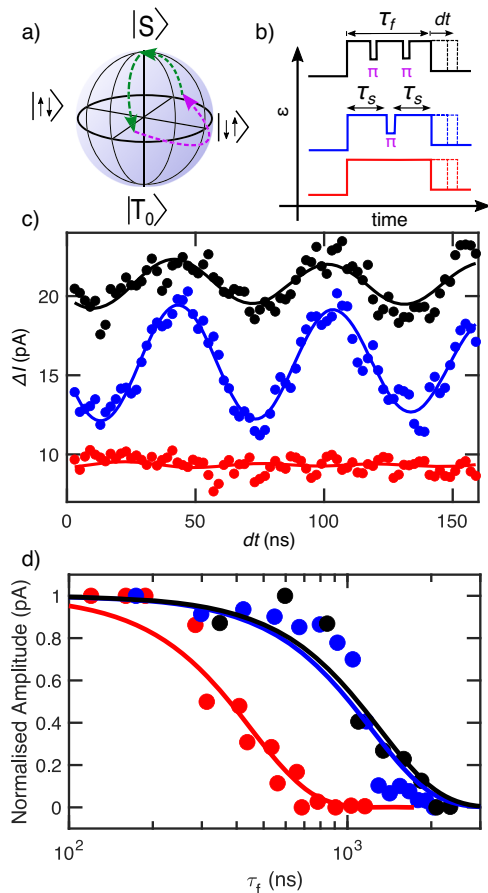
Fig. 5 | Spin-echo measurement at $B_x = 1.6$ mT. a Shows an example trajectory of the qubit-state for the refocusing pulse schematic of (**b**). Free evolution driven by Δg is allowed for a period of time $\tau_S(n) = (2n + 1/2)t_\pi$ (green trajectory), such that after any $\tau_S(n)$, the qubit will be at the equator. A refocusing pulse is incorporated as a π exchange pulse, followed by a second period of free evolution for $\tau_S(n)$. The total time to perform this sequence is the free evolution time, τ_f, which can be varied by increasing n, or repeating the cycle to include multiple refocusing pulses. The full pulse sequence results in the qubit refocusing to $|S\rangle$ after τ_f. **c** Residual $|S\rangle - |T_0\rangle$ oscillations after a free evolution time (τ_f) of 1000 ns for no refocusing pulses (red), one refocusing pulse (blue) and two refocusing pulses (black). **d** Normalised peak-to-peak amplitude of the residual $|S\rangle - |T_0\rangle$ oscillations as a function of free evolution time. For one (blue) and two (black) refocusing pulses, the oscillations are clearly extended compared with the data for no refocusing pulse. The amplitude is normalised against the shortest free evolution for each data set in order to account for the fidelity of the π exchange pulse. We extract T_2^{Echo} based on a fit to the decay envelope of Eqn. (6), using $\alpha = 2$ (see Supplementary Note 5). The experiments were performed for $B_x = 1.6$ mT.

enhance the observed coherence analogous to a Hahn echo. Figure 5a, b show the qubit evolution and pulse sequence for the refocusing procedure, respectively. The spin-echo experiment allowed the qubit to freely evolve for a time t_f, during which N exchange-driven π rotations are carefully interlaced to provide the refocusing echo. Full details of the refocusing procedure are provided in the Methods.

We demonstrate the enhancement of the qubit coherence by observing the residual Δg-driven singlet-triplet oscillations after the free evolution time, t_f. Figure 5c shows the singlet-triplet oscillations after $t_f = 1000$ ns for zero (red), one (blue) and two (black) refocusing pulses. When zero refocusing pulses are applied, the singlet-triplet oscillations are completely lost after 1000 ns of free evolution. However, with refocusing pulses, the singlet-triplet oscillations are visible even after $t_f > 1000$ ns. Figure 5d shows the normalised amplitude of the residual Δg-driven singlet-triplet oscillations observed for a range

of free evolution times. The application of one and two refocusing pulses clearly enhances the coherence of the qubit. We fit the decay of the peak amplitude to extract $T_2^{Echo} = 1220 \pm 150$ ns for one refocusing pulse, and $T_2^{Echo} = 1300 \pm 200$ ns for two refocusing pulses. When no refocusing pulses are applied, we find $T_2^{Echo} = 550 \pm 50$ ns, consistent with the measurements in Fig. 3. Although we see an improvement of 120% by applying one pulse, we see no significant improvement when using two refocusing pulses. This suggests the maximum may have been reached for this simplified refocusing procedure.

In this work we have demonstrated a hole-spin singlet-triplet qubit in planar silicon. We demonstrate rapid $|S\rangle \leftrightarrow |T_0\rangle$ oscillations exceeding 400 MHz, two-axis control via Δg-driven and exchange-driven oscillations, and enhancement of the qubit coherence time to >1 μs using spin-echo procedures. Developing a complete model of the energy spectrum provided insight into spin qubit dynamics under rapid pulses across the $|S\rangle \leftrightarrow |T_-\rangle$ avoided crossing. The experimentally observed effects were well described by the model Hamiltonian. This demonstrates that additional modelling would be useful for simulating new methods to further optimise initialisation protocols in hole-spin qubits, such as identifying optimal magnetic field orientations or simulating more complex pulsing procedures.

We highlight this singlet-triplet qubit is implemented using planar MOS silicon, which is a platform that has future potential for scaling up to large qubit arrays, and implementing surface code error correction[43–45]. Therefore, the results presented here provide a robust foundation for up-scaling hole-spin qubits and offer insights for advancing hole qubit technology further. Furthermore, the analysis regarding the orientation of the spin–orbit vector, the Landau–Zener transitions, and the g-tensor effects are directly relevant to a range of spin qubit systems in silicon, including single spin, exchange only, and hopping qubits[61]. An open question that will impact the future direction of hole-spin qubit technology is the extent of variation of key qubit parameters (such as the g-tensor and spin orbit vector) across different devices, and how well these can be controlled in-situ. Therefore, a future direction for this research is investigating the effects of in-situ controlled operating parameters, such as occupation number and confinement shape, on the qubit operation.

Methods
Sample details
The device was fabricated from high-resistivity natural silicon. The multi-layer Pd gate stack is achieved using 2-nm ALD Al_2O_3 and a high-quality 5.9 nm SiO_2 gate oxide. This device combines nMOS and pMOS capabilities in order to implement a single electron transistor (SET) as the charge sensor, while defining a hole double quantum dot[46,47]. Further details of the device operation are provided in Supplementary Note 1.

Experimental setup
All experiments were performed using a top-loading BlueFors XLD dilution fridge with a three-axis vector magnet. Unless otherwise stated, the experiments were performed with the fridge at base temperature where the mixing chamber thermometer was 40 mK. Previous measurements indicated that at base, this system achieves electron and hole temperatures of 120 mK. The device was fixed directly onto a brass sample enclosure that is thermally anchored to the probe cold-finger. GE varnish was used to mount the device directly onto a brass sample stage, and Al bond wires connected the sample to a homemade printed circuit board. All DC biasing was applied using a Delft IVVI digital-to-analogue converter using lines which each pass through individual 50-kHz low pass filters mounted to the cold-finger (40 mK). The current through the SET was amplified using a Basel SP983c I-V preamplifier. DC currents were then monitored using a Keithly 2000, and standard low-frequency lock-in techniques were implemented using an SR830. For all measurements,

we used an integration time of 100 ms, since any longer integration times did not yield any increase in measured parameters (T_2* or T_{Echo}*).

Rapid pulses were applied to gates P1 and P2 in order to perform initialisation, control and readout out of the singlet-triplet qubit. The pulses were applied using a Tabor WX1284 with 1.25 GS/s. Fast pulses from the WX1284 were routed to gates P1 and P2 using homemade RC bias-tees (R = 330 kOhm, C = 1.2 nF) on the sample PCB at the mixing chamber. The pulses were transmitted from room temperature to the circuit board using coaxial cables with 15 dBm of cold attenuation for thermalisation. Further details of the pulse procedure and spin-to-charge conversion are discussed in Supplementary Notes 2, 3, respectively.

Landau–Zener transitions

Landau–Zener processes are discussed in relation to Fig. 2. The probability of maintaining the initial eigenstate when ramping across an avoided-crossing can be understood in terms of the Landau–Zener transition probability

$$P_{LZ} = \exp\left(\frac{-2\pi\Delta^2}{h\nu}\right), \tag{7}$$

where $\nu = dE/dt$ is the energy level velocity, and Δ is the size of the avoided crossing. For the two-hole-spin system, we initialised a $|S_{2,8}\rangle$, then pulsed (ramp time ≈ 4 ns) to positive detuning. This pulse from negative to positive detuning traverses the $\Delta_{ST_\pm}$ avoided crossing. The magnetic field orientation strongly influences both the magnitude of $\Delta_{ST_\pm}$ and the position in detuning (ϵ_Δ) at which the avoided-crossing occurs. Therefore, the magnetic field orientation impacts the probability of transitioning from $|S_{2,8}\rangle$ into $|T_-\rangle$ during the pulse from (2,8) to (1,9). This in turn influences the amplitude of the $|S\rangle \leftrightarrow |T_-\rangle$ FFT peak (blue), since this peak amplitude is proportional to the probability of occupying $|T_-\rangle$[53]. See Supplementary Note 6 for further discussion of Landau–Zener transitions.

Finally, we comment on the limitations of the Landau–Zener analysis for this experimental procedure. The derivation of the Landau–Zener formula assumes the energy separation term $\nu = dE/dt$ is constant. However, due to the non-linear energy spectrum and the use of a fixed separation pulse (4ns rise time), the term $\nu = dE/dt$ is not constant for our experimental protocol. Therefore, the Landau–Zener picture provides an approximate qualitative understanding of the underlying physics. In order to more accurately capture the dynamics induced by the pulse sequence, we have developed a QuTiP[54] simulation procedure. This procedure allows input of the realistic experimental procedure and the calculation of realistic transition rates (see Supplementary Note 7).

Spin-echo measurement procedure

Here we provide full details of the experimental procedure used for the spin-echo measurement. This procedure was modelled on that developed for a planar Ge singlet-triplet hole-spin qubit[37]. The $|S_{2,8}\rangle$ state was pulsed to large detuning, producing Δg-driven oscillations. We allow a dwell time of $t_S(n) = (2n + 1/2)t_\pi$, where n is an integer and t_π is the time for a Δg-driven π rotation ($t_\pi \approx 60$ ns). Hence, after any $t_S(n)$ the state should be at the equator of the Bloch sphere. After time $t_S(n)$, an exchange-driven π rotation ($t_\pi^J \approx 7$ns) is applied. Following this, we dwell at large separation for a second period $t_S = (2n + 1/2)t_\pi$. Multiple refocusing pulses can be added by repeating the above cycle. The blue schematic in Fig. 5b) shows the sequence for one refocusing pulse, while the black schematic shows the sequence for two refocusing pulses. The free evolution time is the total time of the entire refocusing pulse sequence, $t_f = (2t_S(n) + t_\pi^J)N$, where N is the number of exchange-driven π pulses used. For a fixed number of exchange pulses (N), we can vary the free evolution time by increasing the $t_S(n)$ dwell time. The entire pulse sequence is designed to refocus the qubit to a singlet state, regardless of the total free evolution time $t_f(n)$.

Given that the exchange pulses are shown to enhance coherence in Fig. 5c, it is counterintuitive that the amplitude of the $N = 2$ (black) oscillations are smaller than the $N = 1$ (blue) oscillations in Fig. 5c. However, this is due to the fidelity of the exchange pulse. The fidelity of the exchange pulse reduces the overall amplitude of the oscillations, which is the reason that the amplitude of the two-pulse data (black) is less than the one-pulse data (blue). The limited fidelity restricted the number of refocusing pulses we were able to apply, since, for more than three refocusing pulses, the amplitude of the oscillations were reduced to the noise floor of the singlet-triple visibility, even for short t_f. As a result, we plot the normalised oscillation amplitude in Fig. 5c to allow comparison between the zero, one and two exchange pulse measurements.

Optimal fit for g-tensor and spin–orbit vector

We fit the frequencies of the three FFT peaks in Fig. 2a, c to predicted energy splitting in the singlet-triplet Hamiltonian H_{ST} (defined in Supplement Note 4). This allowed extraction of the g-tensors and spin–orbit vector for this hole-spin qubit. The best fit of the g-tensor for the two dots, is shown in Fig. 6. The spin–orbit vector (three components) and the g-tensors (six components each) result in a very large parameter space, with 16 parameters; t_c, t_x, t_y, t_z, six parameters for g_L and six parameters for g_R. This presents a challenge since the
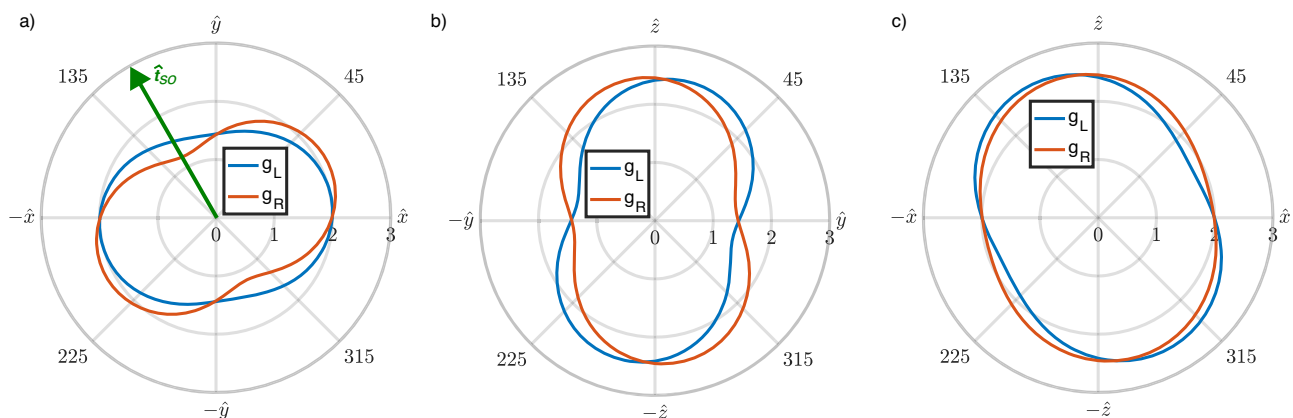

Fig. 6 | Fitting parameters for the g-tensors and spin–orbit vector. a–c The optimal fit g-factors g_L (blue) and g_R (red) plotted as a function of magnetic field orientation. There is a clear misalignment between the principle axes of the left and right g-tensors. The spin–orbit vector is plotted in green in (**a**). We note that while g_L and g_R are used to denote the two distinct g-tensors extracted from the fitting procedure, we are not able to assign either g_L or g_R to a dot under a specific plunger gate.
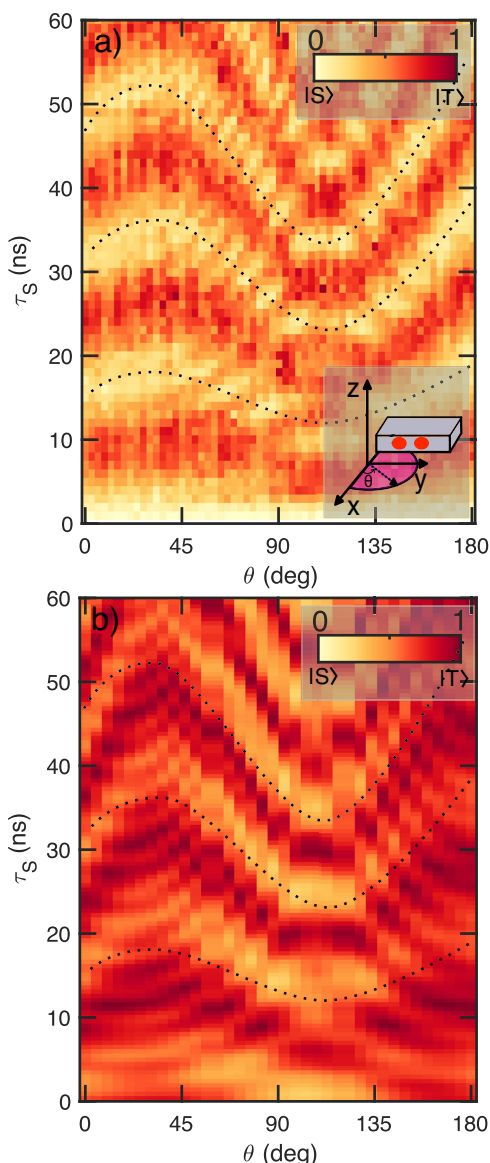
Fig. 7 | Comparison of experimental results and QuTIP Simulation. a The experimental data from Fig. 2c is reproduced over a shortened time scale. The colour scale is the normalised singlet probability. Black dashed lines serve as a guide to the eye for the *Δg*-oscillations. **b** Shows the full simulation of the experimental procedure using the QuTIP model described in Supplementary Notes 7, 8. The black dashed lines are transposed from (**a**). We note that the experiment in (**a**) takes ~3 h to perform and is limited by the integration time of the SRS830 lock-in (0.3 ms). The simulation in (**b**), which uses QuTIP `sesolve` function, takes approximately 10 h to run, and is limited by the number of PC cores running simultaneously.

large number of free parameters prevents the identification of a unique fit to the FFT frequencies alone. In fact, we find more than 50 possible parameter combinations giving good fits to the observed frequencies.

We are able to effectively constrain the fits by simultaneously considering the eigenstate anisotropy and the state occupation probability indicated by the FFT amplitude. This is described in more detail in Supplementary Notes 7, 8. However, the key aspect is that for each potential fit we are able to additionally simulate the probability that the $|S_{2,8}\rangle$ transitions into $|T_-\rangle$ during the 4 ns ramp-in. By combining the two fitting approaches we are able to identify the optimal fit of the hole-spin system. In fact of the ≈50 possible parameter

combinations <10 seemed to show reasonable state occupation probabilities, and one optimal fit was clearly identified (See Fig. 7).

The parameters for the optimal fit are

$$t_c = 13.7 \pm 0.1 \mu eV$$

$$\overleftrightarrow{g}_L = \begin{pmatrix} -0.78 & -1.13 & -1.45 \\ -1.13 & 0.85 & -0.27 \\ -1.45 & -0.27 & 1.91 \end{pmatrix}$$

$$\overleftrightarrow{g}_R = \begin{pmatrix} -0.96 & -0.94 & -1.47 \\ -0.94 & 0.78 & -0.74 \\ -1.47 & -0.74 & 1.82 \end{pmatrix}$$

and

$$\mathbf{t}_{so} = \begin{pmatrix} -37 \pm 2 \\ 107 \pm 4 \\ 0 \pm 20 \end{pmatrix} neV$$

We use labels $\overleftrightarrow{g}_L$ and $\overleftrightarrow{g}_R$ to indicate a 'left' and 'right' g-tensor respectively, however this experiment is unable to assign $\overleftrightarrow{g}_L$ or $\overleftrightarrow{g}_R$ specifically to the P1 or P2 dots. Uncertainty in each of the g-factors was on the order of ±0.02. The optimal fit here provides the parameters used for the solid lines in Fig. 2 of the main text. Figure 6 shows an illustration of the optimal fit g-tensors and spin–orbit vector $\overrightarrow{t}_{so}$. Note that the principle axes of the left and right g-tensor are slightly misaligned with respect to each other.

Optimal fit validation using QuTIP modelling
A key method for validating the optimal fit was a comparison of the experimentally observed qubit dynamics with simulated data tht was generated using the best fit parameters. Figure 7a reproduces the experimental data from Fig. 2c (over a shortened time scale), allowing the non-trivial qubit dynamics to be more clearly identified. At $\theta = 0$ the slower $|S\rangle \leftrightarrow |T_0\rangle$ oscillations are the main component picked up in the FFT data of Fig. 2d. However, as θ increases, additional spectral components become more pronounced, with most significant effects observed at $\theta = 120°$. These additional spectral components arise from both $|S\rangle \leftrightarrow |T_\pm\rangle$ oscillations and $|T_0\rangle \leftrightarrow |T_\pm\rangle$, which both become more prevalent as Δ_{ST} becomes both more open and moves to more positive detuning (See also Fig. 2e).

Figure 7b shows the results of a QuTIP[54] simulation of the experimental procedure. The full details of the modelling procedure are provided in Supplementary Notes 7, 8. For Fig. 7b we use the optimal fit parameters and demonstrate excellent agreement between the simulated and observed qubit dynamics, thus validating the optimal fit parameters. See Supplementary Note 8 for further discussion.

Data availability
The data related to this study have been deposited in the Zenodo database, accessible at https://zenodo.org/records/12803637 and https://github.com/ScottLiles/HoleSTQubit.git.

Code availability
The code generated in this study have been deposited in the Zenodo database accessible at https://zenodo.org/records/12803637 and https://github.com/ScottLiles/HoleSTQubit.git.

References
1. Hornibrook, J. M. et al. Cryogenic control architecture for large-scale quantum computing. *Phys. Rev. Appl.* **3**, 024010 (2015).

2. Veldhorst, M., Eenink, H. G. J., Yang, C.-H. & Dzurak, A. S. Silicon CMOS architecture for a spin-based quantum computer. *Nat. Commun.* **8**, 1766 (2017).

3. Zwanenburg, F. A. et al. Silicon quantum electronics. *Rev. Modern Phys.* **85**, 961 (2013).

4. Loss, D. & DiVincenzo, D. P. Quantum computation with quantum dots. *Phys. Rev. A* **57**, 120 (1998).

5. Burkard, G., Ladd, T. D., Pan, A., Nichol, J. M. & Petta, J. R. Semi-conductor spin qubits. *Rev. Modern Phys.* **95**, 025003 (2023).

6. Levy, J. Universal quantum computation with spin-1/2 pairs and Heisenberg exchange. *Phys. Rev. Lett.* **89**, 147902 (2002).

7. Petta, J. R. et al. Coherent manipulation of coupled electron spins in semiconductor quantum dots. *Science* **309**, 2180–2184 (2005).

8. Maune, B. M. et al. Coherent singlet-triplet oscillations in a silicon-based double quantum dot. *Nature* **481**, 344–347 (2012).

9. Jock, R. M. et al. A silicon metal-oxide-semiconductor electron spin-orbit qubit. *Nat. Commun.* **9**, 1768 (2018).

10. Harvey, S. P. et al. Coupling two spin qubits with a high-impedance resonator. *Phys. Rev. B* **97**, 235409 (2018).

11. Burkard, G., Gullans, M. J., Mi, X. & Petta, J. R. Superconductor–semiconductor hybrid-circuit quantum electrodynamics. *Nat. Rev. Phys.* **2**, 129–140 (2020).

12. Bøttcher, C. G. L. et al. Parametric longitudinal coupling between a high-impedance superconducting resonator and a semiconductor quantum dot singlet-triplet spin qubit. *Nat. Commun.* **13**, 4773 (2022).

13. Spethmann, M., Bosco, S., Hofmann, A., Klinovaja, J. & Loss, D. High-fidelity two-qubit gates of hybrid superconducting-semiconducting singlet-triplet qubits. *Phys. Rev. B* **109**, 085303 (2024).

14. Freer, S. et al. A single-atom quantum memory in silicon. *Quant. Sci. Technol.* **2**, 015009 (2017).

15. Watson, T. F. et al. A programmable two-qubit quantum processor in silicon. *Nature* **555**, 633–637 (2018).

16. Philips, S. G. J. et al. Universal control of a six-qubit quantum pro-cessor in silicon. *Nature* **609**, 919–924 (2022).

17. Undseth, B. et al. Hotter is easier: unexpected temperature depen-dence of spin qubit frequencies. *Phys. Rev. X* **13**, 041015 (2024).

18. Maurand, R. et al. A CMOS silicon spin qubit. *Nat. Commun.* **7**, 13575 (2016).

19. Camenzind, L. C. et al. A hole spin qubit in a fin field-effect transistor above 4 kelvin. *Nat. Electron.* **5**, 178–183 (2022).

20. Watzinger, H. et al. A germanium hole spin qubit. *Nat. Commun.* **9**, 3902 (2018).

21. Hendrickx, N. W. et al. A single-hole spin qubit. *Nat. Commun.* **11**, 3478 (2020).

22. Hendrickx, N. W. et al. A four-qubit germanium quantum processor. *Nature* **591**, 580–585 (2021).

23. Wang, K. et al. Ultrafast coherent control of a hole spin qubit in a germanium quantum dot. *Nat. Commun.* **13**, 206 (2022).

24. Ares, N. et al. Nature of tunable hole g factors in quantum dots. *Phys. Rev. Lett.* **110**, 046602 (2013).

25. Crippa, A. et al. Electrical spin driving by g-matrix modulation in spin-orbit qubits. *Phys. Rev. Lett.* **120**, 137702 (2018).

26. Venitucci, B., Bourdet, L., Pouzada, D. & Niquet, Y.-M. Electrical manipulation of semiconductor spin qubits within the g-matrix formalism. *Phys. Rev. B* **98**, 155319 (2018).

27. Liles, S. D. et al. Electrical control of the g tensor of the first hole in a silicon MOS quantum dot. *Phys. Rev. B* **104**, 235303 (2021).

28. Froning, F. N. M. et al. Strong spin-orbit interaction and g-factor renormalization of hole spins in Ge/Si nanowire quantum dots. *Phys. Rev. Res.* **3**, 013081 (2021).

29. Abadillo-Uriel, J. C. et al. Hole spin driving by strain-induced spin-orbit interactions. *Phys. Rev. Lett.* **131**, 097002 (2023).

30. Sen, A., Frank, G., Kolok, B., Danon, J. & Pályi, A. Classification and magic magnetic-field directions for spin-orbit-coupled double quantum dots. *Phys. Rev. B* **108**, 245406 (2023).

31. Froning, F. N. M. et al. Ultrafast hole spin qubit with gate-tunable spin–orbit switch functionality. *Nat. Nanotechnol.* **16**, 308–312 (2021).

32. Prechtel, J. H. et al. Decoupling a hole spin qubit from the nuclear spins. *Nat. Mater.* **15**, 981–986 (2016).

33. Wang, Z. et al. Optimal operation points for ultrafast, highly coherent Ge hole spin-orbit qubits. *npj Quantum Inf.* **7**, 54 (2021).

34. Bosco, S., Hetényi, B. & Loss, D. Hole spin qubits in Si FinFETs with fully tunable spin-orbit coupling and sweet spots for charge noise. *PRX Quantum* **2**, 010348 (2021).

35. Piot, N. et al. A single hole spin with enhanced coherence in natural silicon. *Nat. Nanotechnol.* **17**, 1072–1077 (2022).

36. Carballido, M. J. et al. A qubit with simultaneously maximized speed and coherence. Preprint at arXiv:2402.07313 (2024).

37. Jirovec, D. et al. A singlet-triplet hole spin qubit in planar Ge. *Nat. Mater.* **20**, 1106–1112 (2021).

38. Jirovec, D. et al. Dynamics of hole singlet-triplet qubits with large g-factor differences. *Phys. Rev. Lett.* **128**, 126 (2022).

39. Sarkar, A. et al. Electrical operation of planar Ge hole spin qubits in an in-plane magnetic field. *Phys. Rev. B* **108**, 245301 (2024).

40. Wang, Z. et al. Electrical operation of hole spin qubits in planar MOS silicon quantum dots. *Phys. Rev. B* **109**, 075427 (2024).

41. Geyer, S. et al. Anisotropic exchange interaction of two hole-spin qubits. *Nat. Physics* **20**, 1152–1157 (2024).

42. Mutter, P. M. & Burkard, G. All-electrical control of hole singlet-triplet spin qubits at low-leakage points. *Phys. Rev. B* **104**, 195421 (2021).

43. Fowler, A. G., Mariantoni, M., Martinis, J. M. & Cleland, A. N. Surface codes: towards practical large-scale quantum computation. *Phys. Rev. A* **86**, 032324 (2012).

44. Hill, C. D. et al. A surface code quantum computer in silicon. *Sci. Adv.* **1**, e1500707 (2015).

45. Li, R. et al. A crossbar network for silicon quantum dot qubits. *Sci. Adv.* **4**, eaar3960 (2018).

46. Jin, I. K. et al. Combining n-MOS charge sensing with p-MOS silicon hole double quantum dots in a CMOS platform. *Nano Lett.* **23**, 1261–1266 (2023).

47. Sousa de Almeida, A. J. et al. Ambipolar charge sensing of few-charge quantum dots. *Phys. Rev. B* **101**, 201301 (2020).

48. Liles, S. D. et al. Spin and orbital structure of the first six holes in a silicon metal-oxide-semiconductor quantum dot. *Nat. Commun.* **9**, 3255 (2018).

49. Studenikin, S. A. et al. Enhanced charge detection of spin qubit readout via an intermediate state. *Appl. Phys. Lett.* **101**, 233101 (2012).

50. Harvey-Collard, P. et al. High-fidelity single-shot readout for a spin qubit via an enhanced latching mechanism. *Phys. Rev. X* **8** 021046 (2018).

51. Winkler, R., Papadakis, S., De Poortere, E. & Shayegan, M. *Spin-Orbit Coupling in Two-Dimensional Electron and Hole Systems* (Springer, 2003).

52. Hung, J.-T., Marcellina, E., Wang, B., Hamilton, A. R. & Culcer, D. Spin blockade in hole quantum dots: tuning exchange electrically and probing Zeeman interactions. *Phys. Rev. B* **95**, 195316 (2017).

53. Petta, J. R., Lu, H. & Gossard, A. C. A coherent beam splitter for electronic spin states. *Science* **327**, 669–672 (2010).

54. Johansson, J. R., Nation, P. D. & Norim, F. Qutip: an open-source python framework for the dynamics of open quantum systems. *Comput. Phys. Commun.* **183**, 1760–1772 (2012).

55. Hanson, R. & Burkard, G. Universal set of quantum gates for double-dot spin qubits with fixed interdot coupling. *Phys. Rev. Lett.* **98**, 050502 (2007).

56. Dial, O. E. et al. Charge noise spectroscopy using coherent exchange oscillations in a singlet-triplet qubit. *Phys. Rev. Lett.* **110**, 146804 (2013).

57. Assali, L. V. C. et al. Hyperfine interactions in silicon quantum dots. *Phys. Rev. B* **83**, 165301 (2011).

58. Wu, X. et al. Two-axis control of a singlet–triplet qubit with an integrated micromagnet. *Proc. Natl Acad. Sci. USA* **111**, 11938–11942 (2014).
59. Pericles, P., Chesi, S. & Coish, W. A. First-principles hyperfine tensors for electrons and holes in GaAs and silicon. *Phys. Rev. B* **101**, 1153021 (2020).
60. Wang, X. et al. Composite pulses for robust universal control of singlet–triplet qubits. *Nat. Commun.* **3**, 997 (2012).
61. Wang, C. A. et al. Operating semiconductor quantum processors with hopping spins. *Science* **385**, 447–452 (2024).
62. Eenink, H. G. J. et al. Tunable coupling and isolation of single electrons in silicon metal-oxide-semiconductor quantum dots. *Nano Lett.* **19**, 8653–8657 (2019).

Author contributions
S.D.L. performed the experiments and analysis. F.E.H. and W.H.L. fabricated the device. Z.W., D.C. and S.D.L. developed the model for H_{ST}. D.J.H. and S.D.L. developed the QuTIP code used to simulate hole-spin dynamics. J.Y.H. and C.C.E. produced the 3D model Fig. 1a. R.S.E and S.D.L. performed fitting of H_{ST}. S.D.L. wrote the manuscript with input from all co-authors. All authors, including A.S., I.K.J., J.H., K.K., I.V., M.J.R., A.S.D. and A.R.H., contributed to the discussion and planning. A.R.H. supervised the project.

Competing interests
A.S.D. is CEO and director of Diraq Pty Ltd. C.C.E., F.E.H., W.H.L. and A.S.D. declare equity interest in Diraq Pty Ltd. The remaining authors declare no competing interests.

Additional information
Supplementary information The online version contains supplementary material available at https://doi.org/10.1038/s41467-024-51902-9.

Correspondence and requests for materials should be addressed to S. D. Liles.

Peer review information *Nature Communications* thanks the anonymous reviewers for their contribution to the peer review of this work. A peer review file is available.

Reprints and permissions information is available at http://www.nature.com/reprints

Publisher's note Springer Nature remains neutral with regard to jurisdictional claims in published maps and institutional affiliations.